Tin-substituted chalcopyrite: an n-type sulfide with enhanced thermoelectric performance

Article

Published Version

It is advisable to refer to the publisher's version if you intend to cite from the work. See [Guidance on citing](#).

To link to this article DOI: http://dx.doi.org/10.1021/acs.chemmater.2c00637

Tin-Substituted Chalcopyrite: An *n*-Type Sulfide with Enhanced Thermoelectric Performance

Sahil Tippireddy, Feridoon Azough, Vikram, Frances Towers Tompkins, Animesh Bhui, Robert Freer, Ricardo Grau-Crespo, Kanishka Biswas, Paz Vaqueiro, and Anthony V. Powell*

ACCESS | 📊 Metrics & More | 📖 Article Recommendations | 🆂�ℐ Supporting Information

ABSTRACT: The dearth of *n*-type sulfides with thermoelectric performance comparable to that of their *p*-type analogues presents a problem in the fabrication of all-sulfide devices. Chalcopyrite ($CuFeS_2$) offers a rare example of an *n*-type sulfide. Chemical substitution has been used to enhance the thermoelectric performance of chalcopyrite through preparation of $Cu_{1-x}Sn_xFeS_2$ ($0 \leq x \leq 0.1$). Substitution induces a high level of mass and strain field fluctuation, leading to lattice softening and enhanced point-defect scattering. Together with dislocations and twinning identified by transmission electron micros-copy, this provides a mechanism for scattering phonons with a wide range of mean free paths. Substituted materials retain a large density-of-states effective mass and, hence, a high Seebeck coefficient. Combined with a high charge-carrier mobility and, thus, high electrical conductivity, a 3-fold improvement in power factor is achieved. Density functional theory (DFT) calculations reveal that substitution leads to the creation of small polarons, involving localized Fe^{2+} states, as confirmed by X-ray photoelectron spectroscopy. Small polaron formation limits the increase in carrier concentration to values that are lower than expected on electron-counting grounds. An improved power factor, coupled with substantial reductions (up to 40%) in lattice thermal conductivity, increases the maximum figure-of-merit by 300%, to $zT \approx 0.3$ at 673 K for $Cu_{0.96}Sn_{0.04}FeS_2$.
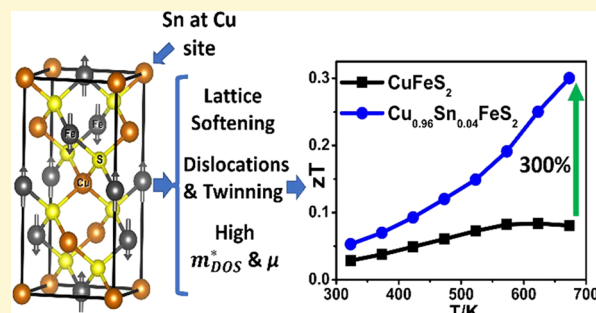
1. INTRODUCTION

Thermoelectric (TE) materials offer the ability to convert waste heat into useful electrical energy and are promising for a range of applications in the automotive, aerospace, manufactur-ing, energy, and electronic industries.[1] The energy conversion efficiency of a thermoelectric material depends on a dimensionless quantity, the figure-of-merit, $zT = S^2\sigma T/\kappa$. For a high zT, the material should possess a high electrical conductivity (σ) and Seebeck coefficient (S), together with a low thermal conductivity (κ). The thermal conductivity comprises electronic (κ_e) and lattice (κ_L) components. However, obtaining a high zT is challenging due to the conflicting dependence of S, σ, and κ_e on the charge-carrier concentration. Using approaches such as doping, nano-structuring, band-structure engineering, and nanocomposit-ing,[2,3] high figures-of-merit have been achieved in many state-of-the-art thermoelectric materials including $PbTe$,[4,5] $SnSe$,[6,7] and Bi_2Te_3.[8,9] However, these materials contain relatively toxic, expensive, and/or rare elements. The search for alternative materials containing relatively abundant and cheap elements has led to the identification of ternary[10−19] and quater-nary[20−23] sulfides, some of which also exist as natural minerals, as promising candidates. However, while this has led to significant improvements in the figure-of-merit of *p*-type

sulfides, there continues to be a dearth of *n*-type analogues with comparable performance.[24]

Among the mineral-related sulfides, chalcopyrite, $CuFeS_2$, has been explored as a potential *n*-type candidate for thermoelectric applications in the mid-temperature ($400 \leq T/K \leq 673$) range. $CuFeS_2$ crystallizes in a tetragonal structure with space group: $I\bar{4}2d$ (Figure 1), which can be considered as a superstructure of the cubic zinc-blende structure, where zinc is replaced by an ordered arrangement of copper and iron cations that occupy tetrahedral $4a$ and $4b$ sites, respectively.[25] It exhibits an antiferromagnetic ground state ($T_N = 823$ K)[26,27] in which the moments of iron cations in consecutive layers in the *c*-direction are aligned in an anti-parallel manner (Figure 1). Pristine $CuFeS_2$ possesses a high Seebeck coefficient ($S \approx -380$ to -480 μV K^{-1} at 300 K) as well as a relatively high electrical resistivity ($\rho \approx 0.25-0.4$ $m\Omega$ m at this temper-ature),[11,28−30] resulting in only a moderate power factor. Moreover, $CuFeS_2$ exhibits a high thermal conductivity ($\kappa \approx 7$
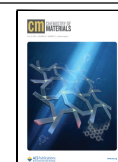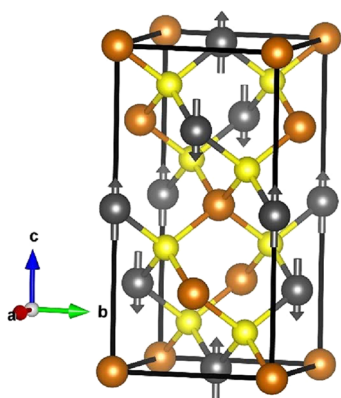
Figure 1. The tetragonal ($I\bar{4}2d$) crystal structure of $CuFeS_2$ where Cu, Fe, and S are denoted by orange, gray, and yellow balls, respectively. The arrows indicate the direction of the individual atomic moments associated with the iron cations, illustrating the anti-parallel arrangement of moments in adjacent layers of iron cations.

to 9 W m^{-1} K^{-1} at 300 K).[11,28−31] Efforts to improve electrical properties have focused on the substitution of Cu$^+$ with higher-oxidation state transition-metal cations, including those of Mn, Co, Ni, Zn, Cd, and Pd,[11,12,30,32] to adjust the carrier concentration and optimize the power factor. The introduction of substituents has also been found to be effective in reducing the lattice thermal conductivity, leading to an improvement in thermoelectric performance.[11,12,30,32] Transition-metal substitution leads to a maximum figure-of-merit $zT = 0.45$ at 723 K[33] for $Cu_{0.88}Ag_{0.12}FeS_2$, the highest achieved in sulfur-based chalcopyrite-related materials, while comparable performance has been reported for $Cu_{0.92}Cd_{0.08}FeS_2$ ($zT = 0.39$ at 723 K).[12] However, Cd is toxic whereas Ag is expensive, thereby making these compositions unsuitable for large-scale production and applications.

Using density functional theory (DFT) calculations for $CuFeS_2$, Park et al.[34] predicted that an optimum charge-carrier concentration of $n \approx 6 \times 10^{21}$ to 8×10^{21} cm^{-3} should lead to a high power factor (≈ 1 mW m^{-1} K^{-2}) and, thus, a high figure-of-merit (~ 0.8 at 700 K for an average grain size of ~ 20 nm). However, $CuFeS_2$ typically has a charge-carrier concentration $ca.$ 10^{19} cm^{-3}, two orders of magnitude lower than the optimum value predicted in that study. In an effort to increase the charge-carrier concentration substantially and more closely approach this optimum carrier concentration, we have substituted copper with tin through the preparation of a series of materials with the general formula $Cu_{1-x}Sn_xFeS_2$ ($0.0 \leq x \leq 0.1$). It has been reported that tin is present in the 4+ oxidation state in ternary and quaternary sulfides including Cu_2SnS_3, $Cu_4Sn_7S_{16}$, Cu_2ZnSnS_4, and Cu_2FeSnS_4.[35−38] Therefore, the substitution of Cu$^+$ with Sn^{4+} potentially introduces more electrons per substituent than in the case of the previously-explored transition-metal substituents with a 2+ oxidation state. Moreover, tin is a relatively cheap and non-toxic element, thus making it a better candidate for large-scale thermoelectric applications. Our results demonstrate that while the 4+ substitution increases the charge-carrier concentration, the increase is lower than expected. Nevertheless, an optimized carrier concentration combined with a high density-of-states effective mass results in a significant increase in the power factor. The substitution also results in lattice softening and enhanced phonon scattering due to lattice strain and generation of point defects. The resulting reduction in thermal

conductivity, coupled with improvements in the power factor, leads to an enhanced figure-of-merit at low levels of tin substitution. The comprehensive analysis of electronic and thermal transport properties of $Cu_{1-x}Sn_xFeS_2$ using a combination of theoretical calculations and experimental data that is reported here suggests an effective strategy to improve the thermoelectric properties of $CuFeS_2$.

2. METHODS

Materials of the general formula, $Cu_{1-x}Sn_xFeS_2$ ($0.0 \leq x \leq 0.1$) were prepared by solid-state synthesis and consolidated by hot pressing. Mixtures of appropriate stoichiometric amounts of Cu (Sigma-Aldrich, 99.5%), Fe (Alfa Aesar, 99%+), and Sn (Alfa Aesar, 99.8%) powders, together with S flakes (Sigma-Aldrich, 99.99%) were transferred to fused silica tubes, which were sealed under a vacuum ($\sim 10^{-3}$ mbar). Reaction mixtures were heated to 723 K and held at this temperature for 150 h before being cooled slowly (0.4 K min^{-1}) to room temperature. The products were ground before refiring in an evacuated fused silica tube at 1173 K for 48 h, followed by slow cooling (0.4 K min^{-1}) to room temperature. The products from the second firing were ground and hot-pressed at 873 K for 30 min under a pressure of 80 MPa to produce pellets for characterization and thermoelectric measurements. The densities of the pellets measured by the Archimedes method, using an AE Adam PW 184 balance, were >97% of the theoretical value.

Powder X-ray diffraction of the final powdered product and hot-pressed samples was carried out using a Bruker D8 Advance diffractometer (Cu K$_{\alpha1}$: $\lambda = 1.5405$ Å), equipped with a LynxEye detector. Powder diffraction data for hot-pressed samples provided no evidence for preferred orientation. Rietveld analysis of the powder diffraction data was performed using FullProf software.[39] X-ray photoelectron spectroscopy (XPS) was performed with a Kratos Axis spectrometer using Al K$_\alpha$ (1486.6 eV) radiation. The spectra were calibrated with C 1s binding energy (B.E. = 284.8 eV), and a Shirley-type background was applied. The peaks were then deconvoluted and fitted with appropriate Lorenz/Gaussian functions using CasaXPS software.

Microstructural investigations were carried out using a SIRION FEI FEG-SEM followed by energy-dispersive X-ray spectroscopy (EDS) elemental point analysis and mapping using a TESCAN MIRA LC FEG (SEM) equipped with an Oxford Instrument SDD energy dispersive detector. Electron backscatter diffraction (EBSD) data were collected using a TESCAN MIRA LC FEG scanning electron microscope (SEM) equipped with an Oxford Instrument SDD EDS detector and an Oxford Instrument Symmetry EBSD detector. Selected-area electron diffraction (SAED) and high-resolution transmission electron microscopy (HRTEM) were performed using an FEI FEGTEM (Tecnai G2, Hillsboro, OR) operating at 300 kV.

The electrical resistivity and Seebeck coefficient on consolidated materials were measured in a direction perpendicular to the pressing direction, over the temperature range $323 \leq T/K \leq 673$ using a Linseis LSR-3 system, while Hall effect measurements were carried out at room temperature using an Ecopia HMS-3000 system. Thermal diffusivity was measured parallel to the pressing direction using a Netzsch LFA-447 NanoFlash instrument ($323 \leq T/K \leq 573$) and an Anter Flashline-3000 system ($573 \leq T/K \leq 673$ K). The thermal conductivity was determined from the diffusivity data using, $\kappa = \alpha C_p d$, where α denotes the thermal diffusivity, C_p is the specific heat capacity, and d is the sample density. The Dulong−Petit equation was used to calculate the specific heat capacity, $C_p = 0.52$ J g^{-1} K^{-1}. The uncertainties for electrical resistivity, Seebeck coefficient, and thermal conductivity are 5, 5, and 10%, respectively. Considering the combined uncertainties of all the measurements, the uncertainty in the calculation of figure-of-merit (zT) is estimated to be ca. 15%. An Epoch 650 Ultrasonic Flaw Detector (Olympus) with a transducer frequency of 5 MHz was used for the longitudinal (v_l) and transverse (v_t) sound velocity measurements at room temperature using disc-shaped consolidated samples.

All the DFT calculations were carried out using the VASP code[40−42] with a projected augmented-wave basis[43] and the generalized gradient approximation (GGA) exchange-correlation functional of Perdew−Burke−Ernzerhof (PBE).[44] In order to account for the strong correlations of the Fe 3d electrons, the Hubbard correction method (GGA + U) was used with the formulation of Dudarev et al.[45] implemented in VASP and an U_{eff} of = 3 eV. The zero-damping DFT-D3 method of Grimme[46] was employed to account for long-range dispersion forces, bringing the lattice parameters in close agreement with the experimentally reported values. A converged plane wave cutoff of 385 eV was used in all the calculations. The tetrahedron method with Blöchl corrections[47] was used to calculate the electronic density of states (DOS). Cell volume, shape and atomic positions for all the structures were fully relaxed using a conjugate gradient algorithm until the forces on each atom fell below 10^{-4} eV Å^{-1}. A fully converged automated Γ-centered k-point mesh was used to define the Brillouin zone. Spin-polarized calculations were performed to include the Fe magnetic moments with antiferromagnetic ordering in $CuFeS_2$ (which was found to be more stable than the ferromagnetic ordering by 0.58 eV per primitive unit cell). The Fe atoms are in a high-spin configuration with a moment of $3.59\mu_B$, in close agreement with the experimental value of $3.67\mu_B$[27] determined using neutron diffraction, and with reported theoretical values of $3.62-3.89\mu_B$.[34,48,49] The tetragonal $CuFeS_2$ in space group $I\bar{4}2d$ was simulated using the optimized lattice parameters $a = b = 5.27$ Å and $c = 10.41$ Å, which are in good agreement with previous theoretical reports[34] and the lattice parameters obtained experimentally in the current study. The harmonic and anharmonic force constants were calculated via the machine-learning regression algorithms implemented in the hiPhive package[50] using settings optimized in a previous study[51] of the thermal conductivities of chalcopyrite-structured semiconductors. The force constants were used to calculate the lattice thermal conductivity using the ShengBTE code.[52]

In the case of Sn-substituted $CuFeS_2$, the small polaron formation scenario where neighboring Fe^{3+} is reduced to Fe^{2+} was simulated by modifying the geometric environment around the substitution site to make it suitable to a reduced Fe species.[53] To do this, we pre-relaxed the configuration after substituting the neighboring Fe atom by an atom that adopts a 2+ state and with a similar ionic radius as Fe^{2+} (we used Zn^{2+}), which is then replaced again by Fe, and the configuration is re-relaxed. The reduction of Fe species was then confirmed by Bader charge analysis.[54,55]

3. RESULTS AND DISCUSSION

Powder X-ray diffraction data (Figure 2) for $Cu_{1-x}Sn_xFeS_2$ ($0 \leq x \leq 0.1$) can be indexed on the basis of a tetragonal unit cell, confirming the presence of a chalcopyrite-related phase throughout the composition range. The low levels of tin
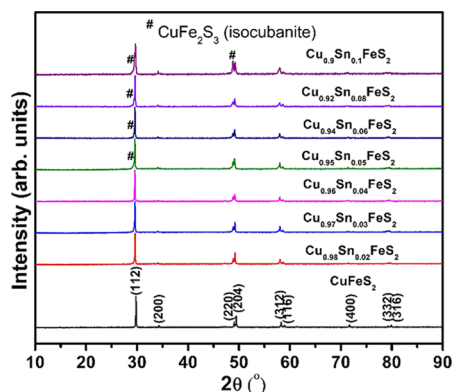

Figure 2. X-ray diffraction patterns of $Cu_{1-x}Sn_xFeS_2$ ($0.0 \leq x \leq 0.1$) samples indexed with the chalcopyrite tetragonal phase.

incorporation, coupled with the similar X-ray scattering powers of copper and iron, make it impossible to establish unambiguously the location of the incorporated tin cations, and therefore, all structural refinements were performed on the basis that tin substitutes at the copper (4a) sites (Figure 3).
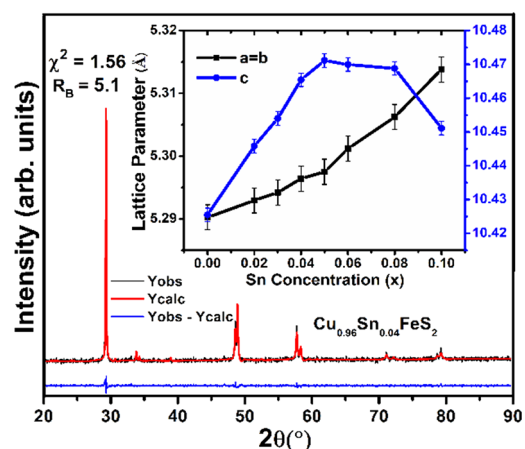

Figure 3. Rietveld analysis of the XRD pattern for $Cu_{0.96}Sn_{0.04}FeS_2$. The inset shows the a (=b) and c lattice parameters as a function of Sn concentration (x).

No reflections arising from secondary phases are observed up to a composition with $x = 0.04$. However, materials with higher tin contents ($x \geq 0.05$) exhibit reflections assignable to a cubic phase identified as $CuFe_2S_3$ (isocubanite), which adopts a structure consisting of a ccp array of anions with a statistical distribution of Cu and Fe cations on half of the tetrahedral sites (Figure S1a). The intensity of the peaks arising from $CuFe_2S_3$ increases with increasing tin concentration (Figure S1b), with volume fractions determined by Rietveld analysis increasing from 8 vol % at $x = 0.05$ to 32 vol % at $x = 0.1$. The compositional variation of lattice parameters evaluated from Rietveld analysis (Figure 3) reveals that the a-lattice parameter increases almost monotonically with increasing tin content, whereas the c-parameter saturates at $x = 0.05$ before decreasing at higher tin contents. This suggests a solubility limit of ca. 4−5 at % of tin, with further increases in tin content resulting in the formation of $CuFe_2S_3$.

The electrical resistivity (ρ) of unsubstituted $CuFeS_2$ (Figure 4a) is ca. 0.31 mΩ m at 323 K and shows a metallic $\rho(T)$ dependence. The Seebeck coefficient of $CuFeS_2$ is negative (Figure 4b), consistent with electrons as the majority charge carriers and the n-type nature of $CuFeS_2$. Despite the metallic $\rho(T)$ dependence, the Seebeck coefficient is high ($S = -430$ μV/K at 323 K) and almost constant up to 573 K. This value is consistent with previous literature reports. However, as is clear from Table S2, there are wide variations in the electrical-transport properties of $CuFeS_2$, with Seebeck coefficients in the range of −320 to −500 μV K^{-1} having been reported. These variations are likely to be associated with slight compositional variations arising from differences in synthesis and processing conditions. The marked decrease in Seebeck coefficient at higher temperatures may be associated with the thermal activation of the minority charge carriers. The low concentration of the minority carriers (holes) results in a low hole contribution to the conductivity, but the hole contribution to the Seebeck coefficient is increased at low carrier contents. The presence of magnetic ions may also
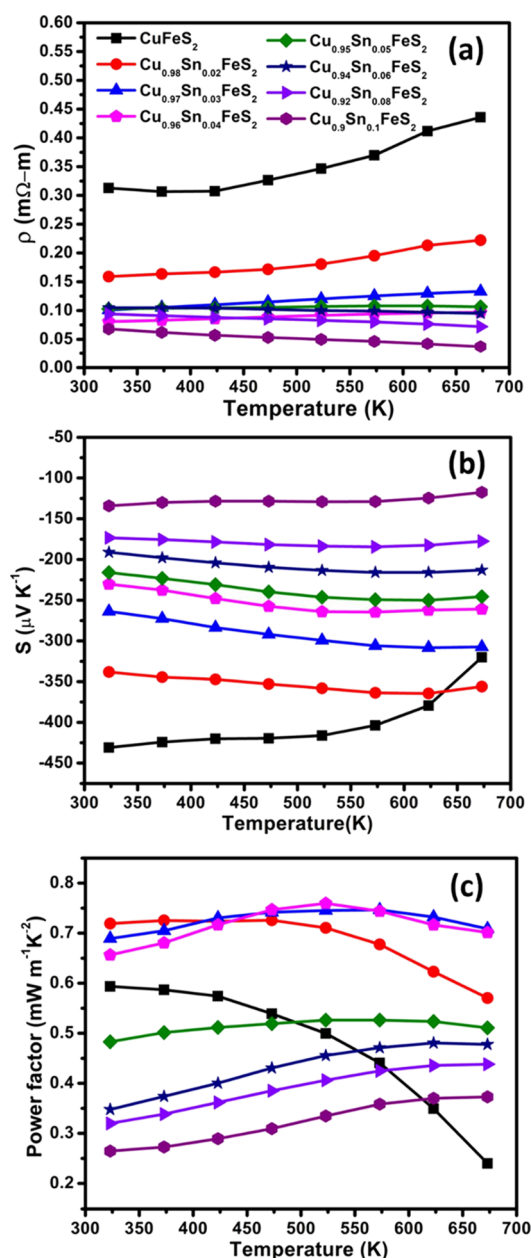
Figure 4. (a) Electrical resistivity (ρ), (b) Seebeck coefficient (S), and (c) power factor (PF) of $Cu_{1-x}Sn_xFeS_2$ ($0.0 \leq x \leq 0.1$) samples as a function of temperature.

influence the $S(T)$ dependence at higher temperatures as the magnetic ordering transition at ca. 800 K is approached, resulting in significant changes in band structure. The metal-like $\rho(T)$ behavior, coupled with a large Seebeck coefficient and high electrical resistivity, indicates degenerate semiconductor behavior and is consistent with previous reports for synthetic $CuFeS_2$.[30,32,33,56]

The electrical resistivity falls markedly on the partial replacement of copper with tin. For example, the electrical resistivity at 323 K is reduced by 50% on the introduction of just 2 at. % of tin in $Cu_{0.98}Sn_{0.02}FeS_2$. The electrical resistivity continues to fall at higher tin contents, although the changes become less pronounced. While pristine $CuFeS_2$ exhibits a sharp decrease in the Seebeck coefficient at ca. 573 K, in contrast, tin-substitution results in a much weaker $S(T)$ dependence and appears to decrease the effect of bipolar

conduction. For a composition with $x = 0.02$, the Seebeck coefficient falls to ca. -340 $\mu V K^{-1}$ at 323 K; a 20% reduction from that of pure $CuFeS_2$, while the electrical resistivity shows an almost 50% reduction at the same temperature. Hence, low levels of tin substitution ($x \leq 0.04$) appear to be more effective in reducing the electrical resistivity compared to the Seebeck coefficient, which contributes to relatively high power factors (Figure 4c). Materials with higher levels of tin incorporation contain increasing amounts of the isocubanite ($CuFe_2S_3$) phase as evidenced by X-ray diffraction. Since the electrical resistivity of isocubanite is an order of magnitude lower ($\rho \approx 0.01$ mΩ m at $323 \leq T/K \leq 723$)[57,58] than that of the $Cu_{1-x}Sn_xFeS_2$ phases, it has an increasingly marked impact on electrical transport properties, effectively decreasing the overall electrical resistivity and significantly modifying its temperature dependence.

The end-member $CuFeS_2$ exhibits a power factor (PF) $ca.$ 0.6 mW m^{-1} K^{-2} at 323 K that falls to 0.24 mW m^{-1} K^{-2} at 673 K, which is primarily due to the decrease in the Seebeck coefficient. At high temperatures, the highest maximum PF $\approx$ 0.7 mW m^{-1} K^{-2} at 673 K was achieved for the $x = 0.03$ and 0.04 samples. However, the weak $S(T)$ dependence shown by the tin-substituted materials results in a much flatter temperature dependence of the power factors, while the magnitude of the power factor is increased. For compositions with $x > 0.05$, although the power factor increases slightly with temperature, the values remain low throughout the measured temperature range.

Room-temperature Hall effect measurements (Table S3) for $Cu_{1-x}Sn_xFeS_2$ ($0.0 \leq x \leq 0.1$) presented in Figure 5a reveal that the charge-carrier concentration of the end-member phase, $CuFeS_2$, is relatively high ($n = 1.4(2) \times 10^{19}$ cm^{-3}), suggesting the existence of defects in the stoichiometric phase, with a mobility, μ, of 15(3) cm^2 V^{-1} s^{-1}. The mobility shows a marked increase on tin substitution, after which it retains a constant value up to $x = 0.05$, before increasing further at higher levels of substitution. The partial replacement of formally Cu^+ with Sn^{4+} leads to an increase in the carrier concentration, as expected. However, a maximum carrier concentration of $n = 3.5(3) \times 10^{19}$ cm^{-3} is reached at $Cu_{0.96}Sn_{0.04}FeS_2$, with the value of carrier concentration decreasing at higher levels of substitution. The maximum carrier concentration achieved was much lower than expected on the basis of electron counting (e.g., ca. 2×10^{21} cm^{-3} for each increment of 0.05 in x). To the best of our knowledge, the carrier mobility of isocubanite has not been reported. However, the lower reported resistivity and Seebeck coefficient of this phase suggests that the mobility is appreciably higher than that of chalcopyrite: a view that is supported by the DFT calculations of Barbier et al.[57,58] Therefore, the presence of appreciable amounts of isocubanite at $x > 0.05$ may contribute to the observed marked increase in the charge-carrier mobility at higher levels of tin substitution. Similar increases in mobility on introduction of a higher mobility phase have been reported in nanocomposites of thermoelectrics.[14,59-61] Carrier scattering due to the presence of a secondary phases becomes significant only when the average mean free path of the carriers is comparable to the dimensions of the secondary phase. DFT calculations[34] show that the average mean free path of the carriers in $CuFeS_2$ is <1 nm, which is much lower than the size of the inclusions of isocubanite (of the order of microns), observed by SEM (Figure S4). Hence, the carrier scattering due to isocubanite is likely to have a small impact on electrical
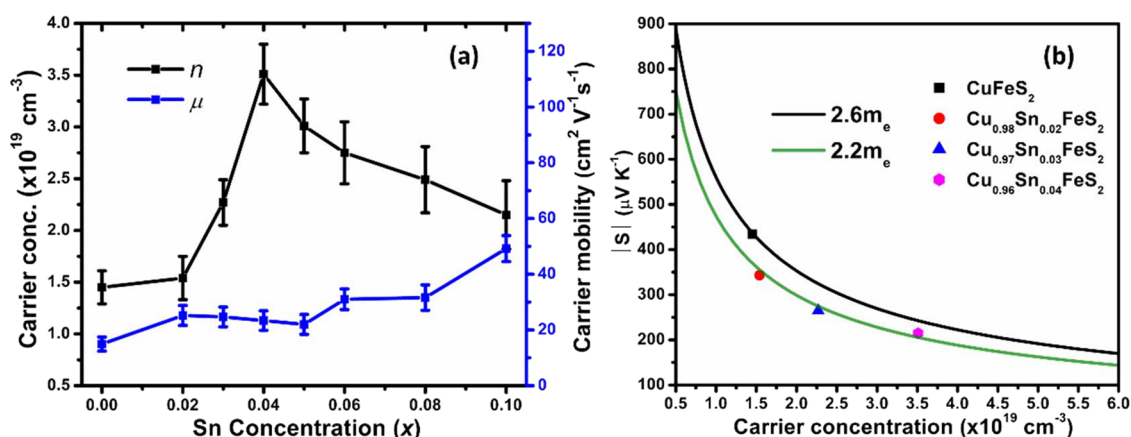
Figure 5. (a) Charge-carrier concentration and mobility of $Cu_{1-x}Sn_xFeS_2$ ($0.0 \leq x \leq 0.1$) samples as a function of Sn concentration (x). (b) Pisarenko plot (S vs n) for $Cu_{1-x}Sn_xFeS_2$ ($0.0 \leq x \leq 0.04$) samples. A comparison with data for other substituted chalcopyrites is presented in Figure S2.
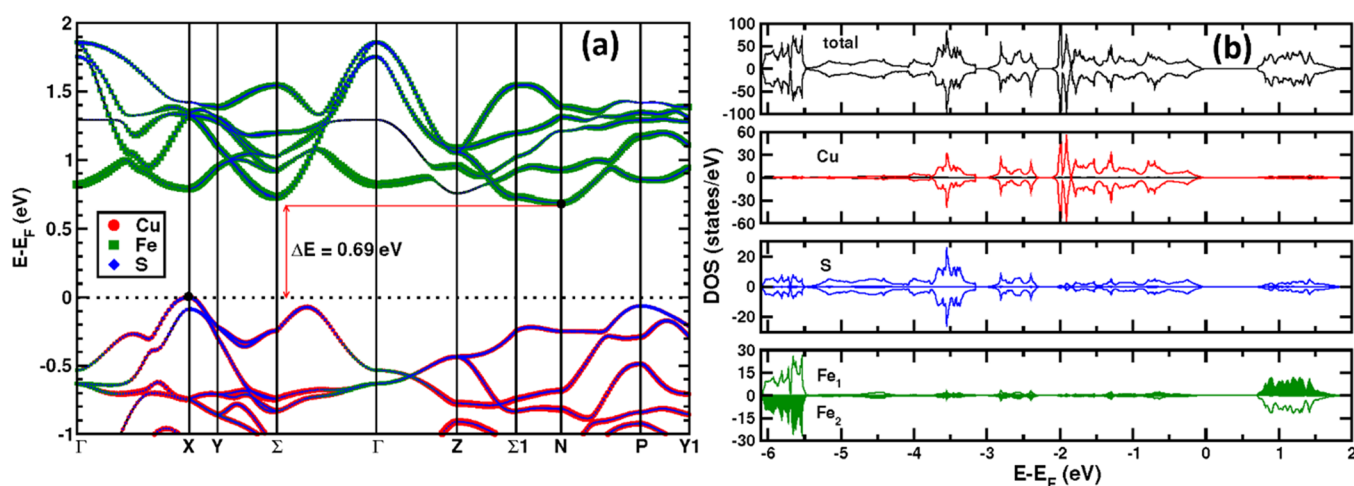

Figure 6. (a) The electronic band structure and (b) the electronic DOS of $CuFeS_2$.

transport properties, given the much higher carrier mobility of this secondary phase.

DFT simulations have been performed in an effort to understand the electrical transport behavior of $CuFeS_2$. Electronic structure calculations (Figure 6a) reveal that the conduction band of $CuFeS_2$ consists primarily of contributions from sulfur $3p$ and iron $3d$ states, while the valence band in the region of the Fermi level (E_F) is principally composed of copper $3d$ and sulfur $3p$ states. There is strong hybridization between the Cu d-states and S p-states as evidenced by the similarity in the partial density of states (DOS) for these states, which is consistent with a strongly covalent Cu−S interaction (Figure 6b). Fe d-states are mostly localized as low-lying valence-band states as well as near-edge conduction-band states, indicating a high degree of ionicity in the Fe−S interaction. The n-type behavior of $CuFeS_2$ identified above implies the presence of intrinsic sulfur vacancies, which serve to move E_F into the conduction band, and suggests that the band structure in the region of the conduction band edge plays a key role in determining the transport properties of $CuFeS_2$. Although there is a clear conduction band minimum (CBM) at the N point, electron pockets exist at the Σ and Z points with energies only 0.04 and 0.06 eV above the CBM, respectively, while the electron pocket at the X point is 0.09 eV higher than the CBM. The close proximity of these electron pockets leads

to a high band degeneracy near the CBM. Band degeneracy is known to enhance the Seebeck coefficients even at low carrier concentrations.[62−64] Combined with the relatively flat nature of the band at the CBM (implying high electron effective mass), this results in the high Seebeck coefficient of pristine $CuFeS_2$ (Figure 4b).

DFT calculations also provide insight into the origin of the lower-than-expected increase in carrier concentration on substitution of copper by tin noted above. In particular, the possibility of formation of an Fe^{3+}-e^{-} bound state (small polaron), corresponding to a reduction of Fe^{3+} to Fe^{2+}, was investigated. Given the limitations of the X-ray diffraction analysis noted above, substitution of tin at both the copper ($4a$) and iron ($4b$) sites was considered. For each mode of substitution, calculations were performed for each of the two possible scenarios: (i) the Fe atom adjacent to the Sn atom is allowed to remain in the Fe^{3+} state (without polaron formation) and (ii) the same Fe atom is "forced" to be in the Fe^{2+} state (with polaron formation). Examination of the ground state energies suggests that in the case of incorporation of Sn at the Cu^{+} site, the polaronic solution is 0.36 eV lower in energy than the non-polaronic solution, i.e., a partial reduction of Fe^{3+} to Fe^{2+} is favored. On the other hand, for Sn substitution at the Fe^{3+} site, the polaronic solution is less stable than the non-polaronic solution by 1.61 eV. This analysis
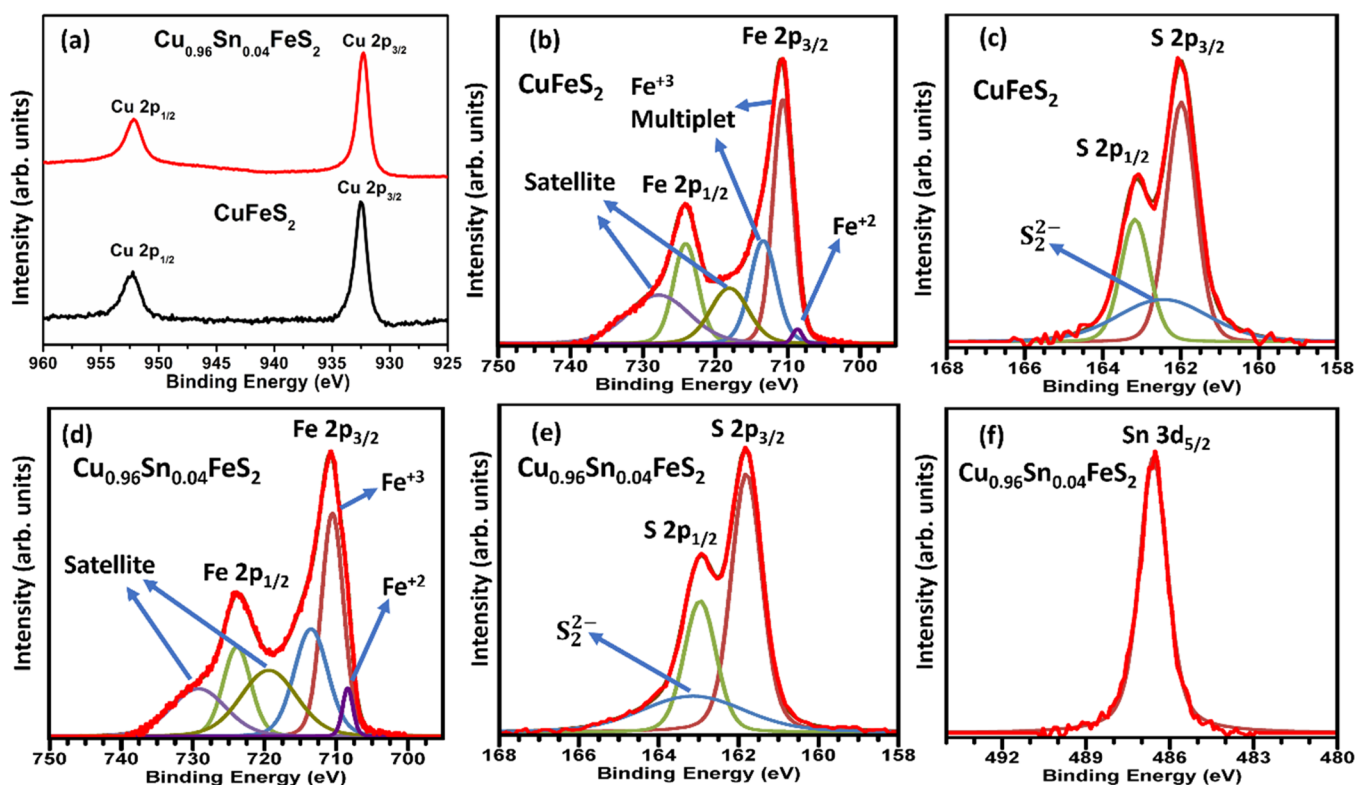
Figure 7. X-ray photoelectron spectroscopy (XPS) spectra of (a) Cu 2p in $CuFeS_2$ and $Cu_{0.96}Sn_{0.04}FeS_2$, (b) Fe 2p in $CuFeS_2$, (c) S 2p in $CuFeS_2$, (d) Fe 2p in $Cu_{0.96}Sn_{0.04}FeS_2$, (e) S 2p in $Cu_{0.96}Sn_{0.04}FeS_2$, and (f) Sn 3d in $Cu_{0.96}Sn_{0.04}FeS_2$.

suggests that polaron formation, which results from substitution of tin at the copper site, may be responsible for the lower-than-expected carrier concentration on substitution. Partial reduction of iron, to form a localized Fe^{2+} state effectively reduces the free carrier concentration and leads to a smaller increase in carrier concentration upon tin substitution (at $x \leq 0.05$) than expected on the basis of replacement of Cu^+ by Sn^{4+}.

Using the charge-carrier concentration (n) determined from Hall measurements, Pisarenko plots were constructed for materials with compositions in the range $0.0 \leq x \leq 0.04$ (Figure 5b). Materials with higher tin contents were not analyzed in this way owing to the presence of significant amounts of an impurity phase, as identified from powder X-ray diffraction. The end-member $CuFeS_2$ phase exhibits a density-of-states (DOS) effective mass, $m_d^* = 2.6\ m_e$, in good agreement with previously reported[30,33,56] values of $m_d^* = 2.2$ to $2.5\ m_e$. The high DOS effective mass contributes to the high Seebeck coefficient and is also consistent with the results of DFT calculations discussed above, where the conduction band was shown to contain multiple pockets with a flat band near the conduction band edge. Tin substitution leads to only a slight decrease in the DOS effective mass to $m_d^* = 2.2\ m_e$ in $Cu_{0.98}Sn_{0.02}FeS_2$. This relatively high value is maintained at low levels of tin substitution, for compositions in the range $0.0 \leq x \leq 0.04$, while an increased carrier concentration and mobility are also retained. The compositional dependence of the Seebeck coefficient is consistent with the behavior described by the Mott formula

$$S = \frac{8\pi^2 k_B^2 T}{3eh^2} m_d^* \left(\frac{\pi}{3n} \right)^{2/3} \qquad (1)$$

where m_d^*, n, e, k_B, and h denote the density-of-states effective mass, charge-carrier concentration, electronic charge, Boltzmann constant, and Planck's constant, respectively. For compositions in the range $0.02 \leq x \leq 0.04$, the DOS effective mass (numerator) is effectively constant, but the charge-carrier concentration (denominator) increases with increasing tin content, resulting in a decrease of the Seebeck coefficient with x. The polaron formation induced by tin substitution reduces the carrier concentration from that expected at a given level of substitution. This enables a relatively high value of the Seebeck coefficient, albeit reduced from that of the end-member phase, to be maintained for levels of tin incorporation of $x \leq 0.04$. Above this value, the isocubanite impurity, which has a much lower Seebeck coefficient ($S = -65$ to $-75\ \mu V\ K^{-1}$ at $323 \leq T/K \leq 723$[57,58] significantly reduces the measured Seebeck coefficient of $Cu_{1-x}Sn_xFeS_2$ ($0.05 \leq x \leq 0.1$). Therefore, although it has been predicted[34] that very high charge-carrier concentrations (ca. 10^{21} cm^{-3}) are required for high electrical performance, when combined with a high DOS effective mass and carrier mobility, comparable power factors can be achieved at significantly lower carrier concentrations (ca. 10^{19} cm^{-3}). This is in agreement with the suggestion of Park et al.[34] that high mobility is a more important factor than carrier concentration in optimizing the power factor and, hence, figure-of-merit of chalcopyrite-derived phases. The high mobility affords a better compromise between Seebeck coefficient and electrical conductivity, enabling optimum performance to be realized at lower doping levels.

X-ray photoelectron spectroscopy (XPS) provides support for the presence of iron in mixed oxidation states, resulting from tin substitution, as predicted by the DFT calculations. Data for the end-member phase, $CuFeS_2$, and for $Cu_{0.96}Sn_{0.04}FeS_2$ exhibit peaks due to Cu^+ (Figure 7a), Fe^{3+}

(Figure 7b,d), and S^{2-} (Figure 7c,e), consistent with the reported formal oxidation states of $CuFeS_2$[11,31,65,66] (Table S4). The deconvoluted tin XPS spectrum for $Cu_{0.96}Sn_{0.04}FeS_2$ (Figure 7f) exhibits a $3d_{5/2}$ peak corresponding to Sn^{4+}. This supports our assertion that tin is incorporated in the 4+ oxidation state, in common with a number of ternary and quaternary sulfides including Cu_2SnS_3, $Cu_4Sn_7S_{16}$, Cu_2FeSnS_4, and Cu_2ZnSnS_4.[35−38] However, in both spectra, a broad weak feature that can be assigned to the persulfide species, S_2^{2-}, is present, together with a second weak feature associated with Fe^{2+}. These peaks may be associated with the presence of trace amounts of a FeS_2 impurity identified by electron microscopy (*vide infra*). However, the intensity of the peak due to Fe^{2+} in the data from the tin-substituted phase, $Cu_{0.96}Sn_{0.04}FeS_2$, is three times higher than that for the end-member phase, $CuFeS_2$. In contrast, the intensity of the persulfide S_2^{2-} peak in the data for $Cu_{0.96}Sn_{0.04}FeS_2$, is only ca. 75% that in $CuFeS_2$. Therefore, our XPS measurements are consistent with the presence of Fe^{2+} in the tin-substituted chalcopyrite phase, as suggested by the DFT calculations, and we propose here that mechanism as the origin of the lower-than-expected increase in carrier concentration on tin substitution.

Scanning electron microscopy images for $Cu_{1-x}Sn_xFeS_2$ for $0.0 \leq x \leq 0.04$ (Figure 8) and for $x > 0.04$ (Figures S3 and S4)
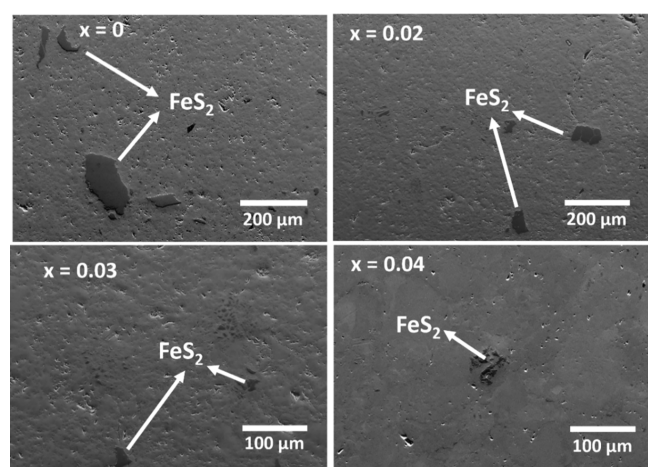

Figure 8. Scanning electron microscopy (SEM) images of $Cu_{1-x}Sn_xFeS_2$ (x = 0, 0.02, 0.03, and 0.04) samples, illustrating the reduction of vol % of FeS_2 phase with an increase in Sn concentration.

reveal a matrix, identified by EDS as the primary chalcopyrite phase, together with a small amount of a secondary FeS_2 phase in all compositions. The FeS_2 impurity can be considered to be the origin of the XPS features assignable to Fe^{2+} and S_2^{2-} in the end-member phase. At higher magnification (Figure S3), trace amounts of Cu_5FeS_4 (bornite) are also discernible in the SEM data, although the formation of this phase is suppressed on substitution by tin. The secondary phases, FeS_2 and Cu_5FeS_4, are present in too low an amount to be detectable by powder X-ray diffraction. For compositions in the range $0.02 \leq x \leq 0.04$, the amount and distribution of the FeS_2 impurity is reduced substantially compared to that in the end-member (x = 0) phase, as was also evidenced in the reduced intensity of the S_2^{2-} peak in the XPS data for the material with a composition corresponding to x = 0.04. This strongly suggests that the increase in the signal from Fe^{2+} in the XPS spectra of the tin-substituted phase is due to the reduction of a fraction of

the Fe^{3+} in the main chalcopyrite phase. For compositions with higher tin contents ($x \geq 0.05$), the SEM data show large amounts of a $CuFe_2S_3$ (isocubanite) type phase (Figure S4), consistent with the powder X-ray diffraction data, in addition to the FeS_2 secondary phase, while in $x \geq 0.08$ samples, bornite is also evident at the periphery of the isocubanite phase (Figure S4). Tin substitution has no significant impact on the morphology for compositions of $x \leq 0.04$ but at higher levels of substitution ($x \geq 0.05$), a high concentration of microcracks and pores are observed. The compositions of the primary chalcopyrite-type phase in the series $Cu_{1-x}Sn_xFeS_2$ were determined from EDS data (Table S5). The experimentally determined compositions are broadly in line with the nominal compositions. The slight Cu excess may be a consequence of the overlap of the K_α and L_α characteristic lines of Cu and Fe (from both the main $CuFeS_2$ and secondary FeS_2 phases), while the tin content agrees well with the nominal values.

The thermal conductivity of the end-member phase, $CuFeS_2$, is relatively high (ca. 6.7 W m^{-1} K^{-1} at 323 K), similar to reported values of ∼6.5−8 W m^{-1} K^{-1} (at 323 K),[11,12,30,33,67] but is substantially reduced on substitution of copper by tin (Figure 9a). The electronic contribution to the thermal conductivity (details of the calculation of κ_e are provided in the Supporting Information) is typically *ca.* 1−10% (for $0.0 \leq x \leq 0.04$ at 673 K) of the total thermal conductivity. Therefore, the thermal conductivity of materials in the series $Cu_{1-x}Sn_xFeS_2$ is mainly due to the lattice contribution (κ_L), and the reduction of 20−40% in the observed thermal conductivity
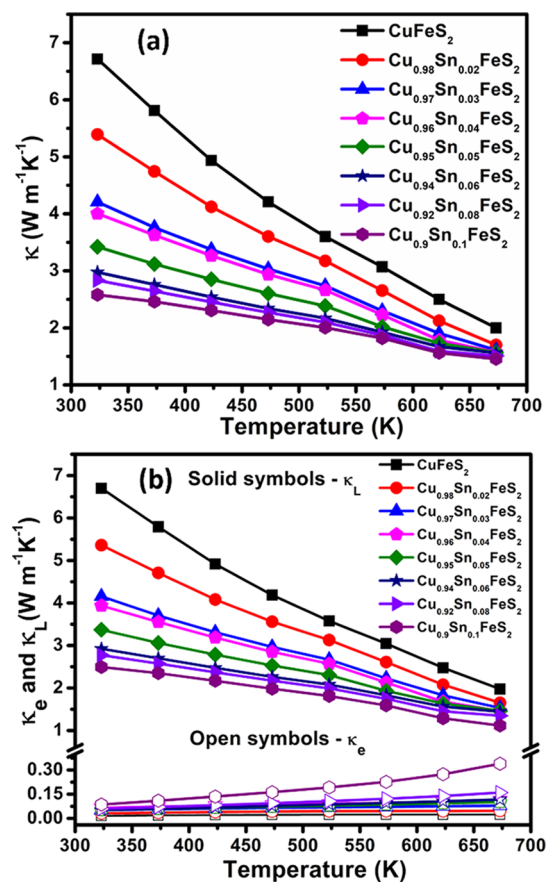

Figure 9. (a) Total (κ), (b) electronic (κ_e), and lattice (κ_L) thermal conductivities of $Cu_{1-x}Sn_xFeS_2$ ($0.0 \leq x \leq 0.1$) samples as a function of temperature.

for substituted phases over the range $0.02 \leq x \leq 0.04$, is primarily due to a reduction in κ_L (Figure 9b).

Sound velocity measurements (Table 1) were conducted for $Cu_{1-x}Sn_xFeS_2$ with compositions corresponding to $x = 0$, 0.02,

Table 1. Various Physical Parameters for $Cu_{1-x}Sn_xFeS_2$ ($x = 0$, 0.02 and 0.04) Samples Showing the Longitudinal (v_l), Transverse (v_t), Average (v_{avg}), and Mean (v_m) Sound Velocities, Young's (E) and Shear (G) Moduli, and Debye Temperature (θ_D)

sample	v_l (m/s)	v_t (m/s)	v_{avg} (m/s)	v_m (m/s)	E (Gpa)	G (Gpa)	θ_D (K)
$x = 0$	4720	2536	3264	2831	69.9	26.94	319
$x = 0.02$	3850	2245	2780	2490	50.59	20.36	280
$x = 0.04$	3500	2150	2600	2372	45.03	18.81	267

and 0.04. In common with previously reported values,[31,67] the end-member phase, $CuFeS_2$, exhibits a high mean sound velocity (Table 1) of $v_m = 2831$ m s^{-1}, accounting for the high measured lattice thermal conductivity, κ_L. On tin substitution, the mean sound velocity is markedly reduced, which is reflected in the significant reduction of κ_L for the tin-substituted materials (Figure 9b). The Debye temperature and elastic modulus, derived from the sound velocity measurements (details of the calculation are provided in the Supporting Information), show corresponding reductions on substitution of copper with tin.

Calculation of the phonon dispersion (Figure 10a) and phonon density-of-states (PDOS) for $CuFeS_2$ (Figure 10b) reveal that the majority of the low frequency (<3 THz) heat-carrying acoustic phonon modes lie below 8−12 meV. The

average group velocity of these acoustic modes is relatively high (3448 m s^{-1} along $\Gamma - X$ and 3400 m s^{-1} along $\Gamma - Z$) and is responsible for the high mean sound velocity and lattice component of the thermal conductivity. It can be seen from Figure 10b that copper vibrations are the biggest contributor to the acoustic phonons. The low-energy optical modes with frequencies in the range of 4 to 6 THz arise from both Cu and Fe atoms vibrating inside their tetrahedra with almost fixed S positions, whereas the high-frequency (8−11 THz) optical modes are dominated by the motion of S atoms, involving considerable bond stretching.

The frequency dependence of the phonon mean free paths reveal that at 300 K, the majority of the transverse and longitudinal acoustic modes have a mean free path between 50 and 500 nm (Figure 10c). At 700 K, the mean free paths reduce to ~20−200 nm. We have calculated the effect of nanoparticle and/or grain boundary size on κ_L (Figure 10d). This calculation was performed by imposing a cut-off on the mean free path of the phonons. Phonons with a longer mean free path than the cut-off are considered to be scattered, leading to a reduction in κ_L. At 300 K, a small population of phonons can be scattered effectively for a nanoparticle/grain boundary size of ~500−600 nm, reducing κ_L by ca. 20%. However, the particle size required for a given relative decrease of κ_L reduces with increasing temperature. For example, at 700 K, the same 20% reduction would require a nanoparticle/grain boundary size of ~200 nm. Therefore, in order to achieve the 20 to 40% reduction of κ_L at higher temperatures, which is observed experimentally (Figure 9b) for $Cu_{1-x}Sn_xFeS_2$ ($0.02 \leq x \leq 0.04$) samples, the nanoparticle/grain boundary size should be <100 nm.
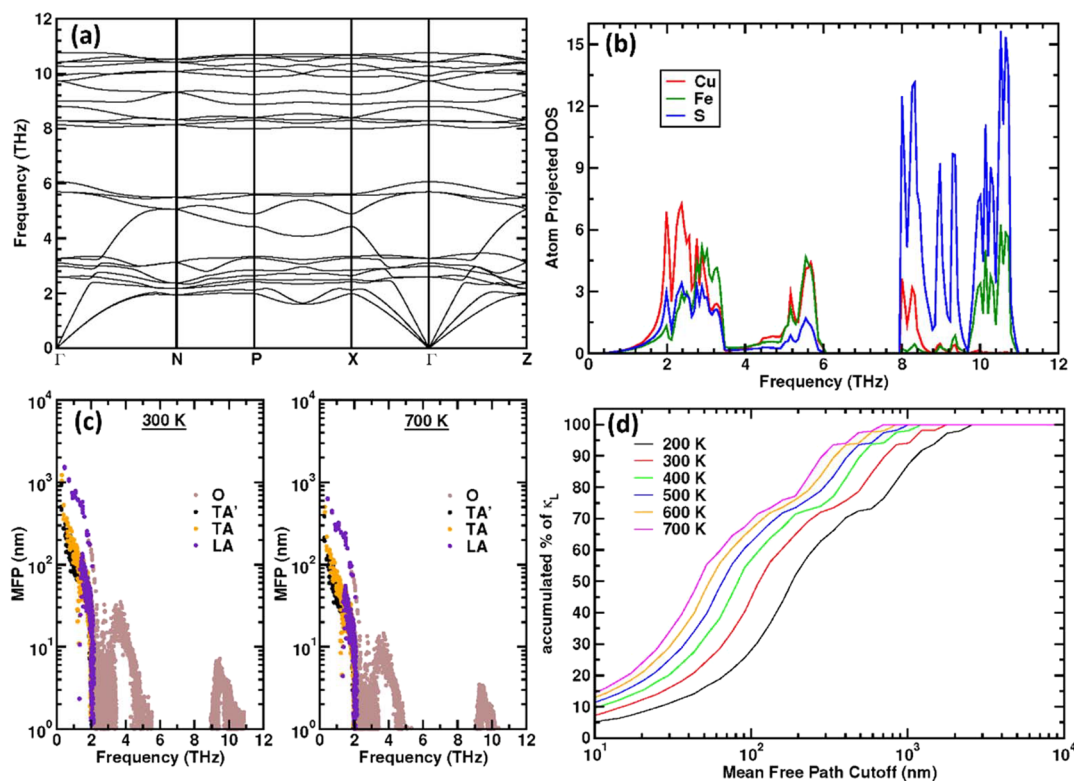

Figure 10. The phonon (a) dispersion curve and (b) DOS of $CuFeS_2$. (c) The mean free path (MFP) of optical (O), transverse acoustic (TA) and longitudinal acoustic (LA) phonon modes at 300 and 700 K. (d) The accumulated percentage of lattice thermal conductivity (κ_L) as a function of mean free path cut-off at different temperatures.

High-resolution transmission electron microscopy (HRTEM) was used to investigate the micro- and nano-structural features of $Cu_{0.96}Sn_{0.04}FeS_2$ that may have an impact on the mean free path of heat-carrying acoustic phonons. The [110] zone HRTEM image (Figure 11a) of the chalcopyrite
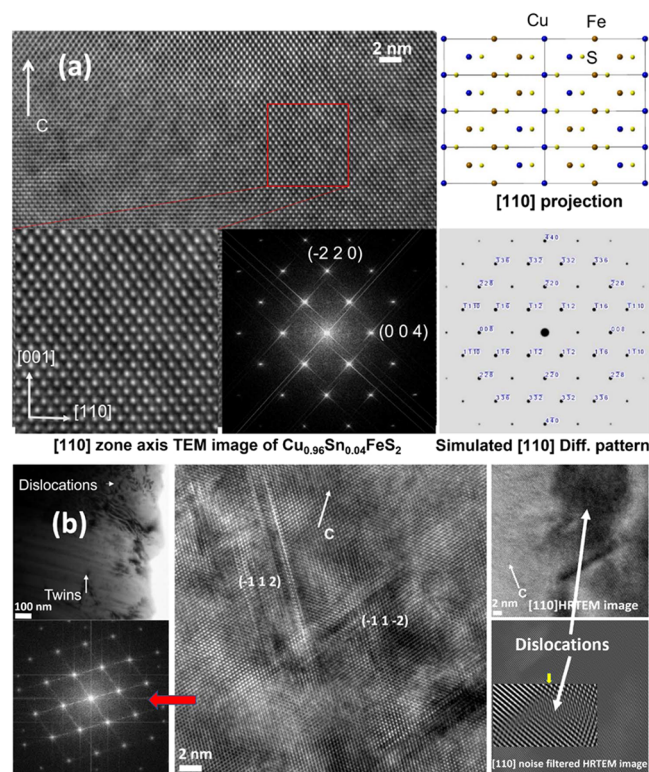

Figure 11. (a) Transmission electron microscopy (TEM) images of the Sn-substituted $Cu_{0.96}Sn_{0.04}FeS_2$ with the selected area electron diffraction (SAED) pattern confirming the tetragonal structure of chalcopyrite. (b) High-resolution TEM images showing dislocations and twinning of the {112} planes.

phase in $Cu_{0.96}Sn_{0.04}FeS_2$ shows uniform atomic ordering with no short-/long-range disordered domains. The selected area electron diffraction (SEAD) pattern was matched to the simulated diffraction spots of the chalcopyrite structure along the [110] projection. The absence of additional Bragg spots and/or any spot splittings rules out superstructures or lower-symmetry structures, respectively, and confirms that the tetragonal $I\bar{4}2d$ crystal structure, on which the powder X-ray diffraction data were interpreted, persists into the tin-substituted phases. However, a bright/dark contrast is observed in the HRTEM image (Figure 11b), indicative of dislocations in some grains and grain boundaries. Moreover, a twinning of the {112} plane is observed, as has been found previously in substituted $CuFeS_2$ compounds.[32] Murr et al.[68] attributed this to the similarity of the tetragonal $CuFeS_2$ to the cubic zinc-blende structure in which twinning of the {111} plane is a typical feature and occurs frequently. Therefore, the

superstructures of cubic phases (of which chalcopyrite is one example), with the c/a ratio approaching 2, exhibit similar twinning since the {112} plane of $CuFeS_2$ is analogous to the {111} plane of the zinc-blende. In the case of $Cu_{0.96}Sn_{0.04}FeS_2$, $c/a = 1.976$, and therefore, twinning is to be expected. These dislocations and twinning features are on the length scale of 10−50 nm and, hence, on the basis of the calculations discussed above, are expected to scatter acoustic phonons. Electron backscattering diffraction (EBSD) data for $Cu_{0.96}Sn_{0.04}FeS_2$ reveals a multiscale grain size distribution (Figure S5) with grain sizes ranging from one to several microns. However, our calculations suggest that since these grains have much larger sizes than the mean free path of the acoustic phonons, they are unlikely to have significant impact in reducing the lattice thermal conductivity.

In order to understand the mechanism behind the reduced lattice thermal conductivity in tin-substituted samples, the Debye−Callaway model[69,70] was fitted to the experimentally measured thermal conductivities. According to this model, the lattice thermal conductivity can be written as[69,70]

$$\kappa_L = \frac{k_B}{2\pi^2 v_m}\left(\frac{k_B T}{\hbar}\right)^3 \int_0^{\theta_D/T} \frac{x^4 e^x}{\tau_c^{-1}(e^x - 1)^2}dx \tag{2}$$

where $x = \hbar\omega/k_B T$, k_B is the Boltzmann's constant, $\hbar$ is the reduced Plank's constant, ω is the phonon frequency, v_m is the mean sound velocity, θ_D is the Debye temperature, and τ_c^{-1} is the total phonon relaxation rate given by

$$\tau_c^{-1} = \tau_B^{-1} + \tau_D^{-1} + \tau_U^{-1} = \frac{v_m}{L} + A\omega^4 + B\omega^2 Te^{-\theta_D/3T} \tag{3}$$

which considers contributions from grain boundary (τ_B^{-1}), point defect (τ_D^{-1}), and phonon−phonon Umklapp (τ_U^{-1}) scattering processes. In eq 3, L is the average grain size, and A and B are the fitting parameters, which, respectively, are a measure of the contributions of the point defect and Umklapp scattering processes. The fitted parameters (Table 2) reveal that while the Umklapp contribution shows little change with increasing levels of tin substitution, the point defect scattering contribution increases significantly. Since copper cations within the CuS_4 tetrahedral network are primarily responsible for the heat-carrying acoustic modes (*vide supra*), the substitution by tin, which has a higher mass and larger atomic radius, can lead to significant local disorder and, therefore, point defect scattering of these acoustic modes. The effect of this disorder can be quantified by formulating the coefficient, A, in terms of the following expression:

$$A = \frac{\Omega_o}{4\pi v_m^3}\Gamma \tag{4}$$

where, Ω_o is the volume of the primitive unit cell and Γ is the scattering parameter. Using the model of Slack[71] and Abeles,[72] the scattering parameter Γ can be written as $\Gamma = \Gamma_M + \Gamma_S$,

Table 2. Extracted Scattering Parameters from the Debye−Callaway Model for $Cu_{1-x}Sn_xFeS_2$ ($x = 0$, 0.02 and 0.04) Samples

sample	L (μm)	A ($\times 10^{43}$ s^{-3})	B ($\times 10^{43}$ s^{-3})	Γ ($\times 10^{-3}$)	Γ_M ($\times 10^{-3}$)	Γ_S ($\times 10^{-3}$)	ε
$x = 0$	12.1	2	6				
$x = 0.02$	9.9	10.24	6.2	10.86	7.08	3.78	68
$x = 0.04$	5.4	43.66	6	39.91	13.88	26.03	242

where Γ_M and Γ_S are the scattering parameters for mass-difference and strain field fluctuations, respectively, given by

$$\Gamma_M = \frac{\sum_{i=1}^{n} c_i \left(\frac{\overline{M_i}}{\overline{M}}\right)^2 f_i^2 f_i^2 \left(\frac{M_i^1 - M_i^2}{\overline{M_i}}\right)^2}{\sum_{i=1}^{n} c_i} \quad (5)$$

and,

$$\Gamma_S = \frac{\sum_{i=1}^{n} c_i \left(\frac{\overline{M_i}}{\overline{M}}\right)^2 f_i^2 f_i^2 \, \varepsilon \left(\frac{r_i^1 - r_i^2}{\overline{r_i}}\right)^2}{\sum_{i=1}^{n} c_i} \quad (6)$$

where $\overline{M_i} = \sum_k f_i^k M_i^k$, $\overline{r_i} = \sum_k f_i^k r_i^k$, and $\overline{M} = \frac{\sum_{i=1}^{n} c_i \overline{M_i}}{\sum_{i=1}^{n} c_i}$. Here, n is the number of crystallographic sub-lattices which is 3 for $CuFeS_2$ and c_i is the degeneracy of each site in the primitive unit cell ($c_1 = c_2 = 1$, $c_3 = 2$ corresponding to Cu, Fe, and S sites, respectively). $\overline{M_i}$ and $\overline{r_i}$ denote the average mass and radius of the atoms on the ith sublattice, respectively. M_i^k and f_i^k are the atomic mass and fractional occupation of the kth atom on the ith sublattice, respectively. $\overline{\overline{M}}$ is the total average atomic mass of the compound. Finally, ε is a phenomenological adjustable parameter that was evaluated from fitting eq 2 to the experimental κ_L. For $Cu_{1-x}Sn_xFeS_2$ samples, on the basis of tin substitution occurring at the copper site, as established above, the total scattering parameter can be thus written as

$$\Gamma = \frac{1}{4}\left(\frac{\overline{M}_{Cu}}{\overline{M}}\right)^2 x(1-x) \left[\left(\frac{M_{Cu}^{Cu} - M_{Cu}^{Sn}}{\overline{M}_{Cu}}\right)^2 \right.$$
$$\left. + \varepsilon \left(\frac{r_{Cu}^{Cu} - r_{Cu}^{Sn}}{\overline{r}_{Cu}}\right)^2\right] \quad (7)$$

The extracted scattering parameters from substituting the coefficient A in eq 2 and fitting the expression to the experimental κ_L are shown in Table 2, where it can be seen that both the mass and strain field fluctuation scattering increase with an increase in the tin content. In previous work with transition metals, such as zinc substitution at the copper site,[11] it was found that only the strain field fluctuation contributes to the reduction in the lattice thermal conductivity because of the similar atomic masses of Zn and Cu. However, tin having a much higher atomic mass (118.71 amu) compared to Cu (63.546 amu) also introduces a considerable contribution from mass-difference fluctuation scattering. Interestingly, at a low level of tin substitution ($x = 0.02$), the scattering is dominated by the mass-fluctuation term (Γ_M), but for $x = 0.04$, the strain field (Γ_S) scattering term becomes much larger compared to Γ_M. Clearly, higher levels of tin substitution induce a significant strain in the lattice.

The reduced elastic moduli and Debye temperature (derived from the sound velocity data shown in Table 1) in the tin-substituted materials compared to $CuFeS_2$ further confirm that the local strain fluctuation caused by tin results in a significant lattice softening. Comparing the Γ values of $Cu_{0.96}Sn_{0.04}FeS_2$ determined in the present study with those obtained at similar levels of substitution (2−4 at %) of Zn[11] and Cd[12] at the Cu site reveals that the total scattering parameter is much larger in the present case as both Γ_M and Γ_S have significant contributions. These point defects, combined with a small contribution from the dislocations and twinning faults, observed in the HRTEM data result in effective scattering of

phonons over a wide range of the acoustic phonon spectrum. For higher levels of substitution ($x \geq 0.05$), κ_L decreases further through a combination of these effects and the increased amount of impurity phases. The thermal conductivity of isocubanite, identified by powder X-ray diffraction, is somewhat lower than that of chalcopyrite ($\kappa_L \approx 3.6$ to 2.5 W m^{-1} K^{-1} over the range $323 \leq T/K \leq 673$)[57,58] and therefore contributes to the reduction in thermal conductivity of the more highly substituted materials. Moreover, for materials with $x > 0.05$, the microstructure consists of a high concentration of pores and microcracks. The combination of these factors produces strong phonon scattering for compositions with $x \geq 0.05$ samples, the lowest lattice thermal conductivity ($\kappa_L \approx 1.45$ W^{-1} m^{-1} K^{-1} at 673 K) being observed for the $x = 0.1$ composition.

The relatively low maximum thermoelectric figure-of-merit ($zT \approx 0.08$ at 673 K) of the end member-phase $CuFeS_2$ (Figure 12) is due to a combination of a high electrical
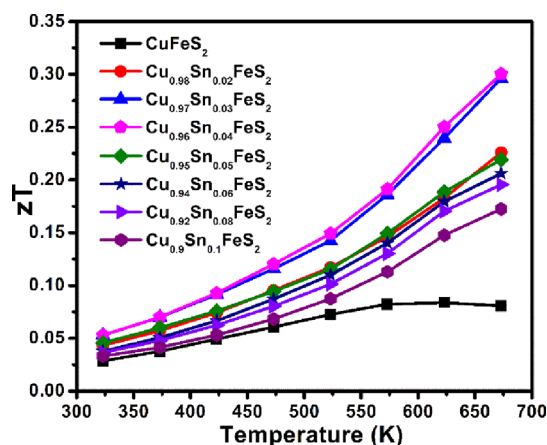

Figure 12. Thermoelectric figure-of-merit (zT) of $Cu_{1-x}Sn_xFeS_2$ ($0.0 \leq x \leq 0.1$) samples as a function of temperature.

resistivity and a high lattice thermal conductivity. However, the almost 3-fold increase in power factor at low levels of tin substitution, principally due to the combination of an optimum charge-carrier concentration and high DOS effective mass (m_d^*), coupled with marked reductions in thermal conductivity, leads to a significant increase in the figure-of-merit. The maximum figure-of-merit of $zT \approx 0.3$ achieved at 673 K in $Cu_{0.96}Sn_{0.04}FeS_2$ is more than 3 times higher than that of the end-member $CuFeS_2$ and is larger than that of the majority of the previously reported substituted $CuFeS_2$ phases.[11,28,30,32,56] As noted previously, the thermoelectric performance of n-type sulfides is inferior to that of their p-type counterparts. Achieving high performance in n-type analogues is of paramount importance for the construction of an all-sulfide TE device containing chemically compatible components. The maximum figure-of-merit reported in this work compares favorably with previous reports of n-type sulfides (Figure 13). Moreover, the level of performance in the chalcopyrite-derived phase reported here is achieved in a material containing cheap and abundant elements. This offers clear advantages over materials containing rarer elements such as silver, which outweigh the slightly higher performance of the latter.
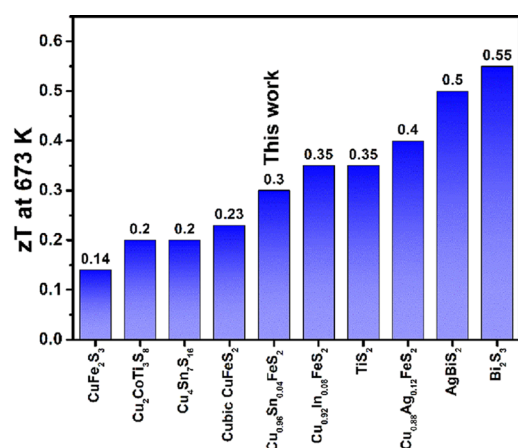
Figure 13. A comparison of the thermoelectric figure-of-merit (zT) at 673 K of potential *n*-type sulfide-based materials.[19,33,57,73−78]

4. CONCLUSIONS

The impact on the structural, electronic, and thermoelectric properties of $CuFeS_2$ of substitution of copper by tin has been investigated using a range of experimental and computational methods. The solubility limit of Sn was found to be ca. 4 at. %, beyond which an isocubanite secondary phase is observed. While it is not possible to establish the mode of substitution directly by powder X-ray diffraction, the combination of DFT calculations and XPS measurements indirectly support the interpretation that tin preferentially replaces copper at the 4*a* sites. The DFT calculations reveal that substitution of Cu^+ by Sn^{4+} leads to small polaron formation. This arises from the partial reduction of Fe^{3+} to form localized Fe^{2+} states, which is consistent with the reduction of iron that is observed by XPS. In contrast, DFT predicts that replacement of Fe by Sn would not result in Fe reduction and would therefore be inconsistent with the XPS results.

Polaron formation leads to a lower-than-expected increase in the charge-carrier concentration. Nevertheless, the charge-carrier concentration of $CuFeS_2$ is still increased through substitution with tin. While this is reduced from the 3 electrons per substituent that would be expected on the basis of formal charges, the increase in charge-carrier concentration results in a reduction in electrical resistivity. Significantly, this occurs with the retention of a high density-of-states effective mass, which results in a relatively high Seebeck coefficient being maintained. This combination of a low resistivity and high Seebeck coefficient results in a high power-factor (ca. 0.7 mW m^{-1} K^{-2} for $Cu_{0.96}Sn_{0.04}FeS_2$ at 673 K) at modest levels of substitution. This demonstrates the effectiveness of relatively small changes in carrier concentration, similar to that reported for a number of chalcogenide systems.[33,79−81] Furthermore, the power factor shows a very weak temperature dependence. The nearly flat PF(T) response may be an attractive feature for device performance.

Tin substitution also leads to lattice softening and enhanced phonon scattering due to both mass and strain field fluctuations. This, in combination with dislocations and twinning faults, results in a substantial reduction in the lattice thermal conductivity, demonstrating the effectiveness of tin substitution as a promising strategy to increase the phonon scattering across different length scales and improve the thermoelectric performance. On the basis of the calculated accumulated percentage of lattice thermal conductivity (κ_L) as

a function of mean free path (Figure 10d), increasing phonon scattering, particularly for those with mean free paths in the range 50−500 nm, is a key element in the design of new high-performance *n*-type chalcopyrite materials. In the present work, we have shown that the reductions in thermal conductivity achieved through lattice softening, together with the high power factor, results in a maximum figure-of-merit $zT = 0.3$ at 673 K for $Cu_{0.96}Sn_{0.04}FeS_2$. This represents a more than 3-fold increase over that of the parent phase, suggesting that $Cu_{1-x}Sn_xFeS_2$ materials may indeed hold promise as candidates for thermoelectric applications in the mid-temperature range.

■ ASSOCIATED CONTENT

ⓢ Supporting Information

The Supporting Information is available free of charge at https://pubs.acs.org/doi/10.1021/acs.chemmater.2c00637.

Crystal structure of isocubanite secondary phase and XRD patterns of $Cu_{1-x}Sn_xFeS_2$ ($x = 0.05−0.1$) showing an increase in isocubanite peaks with *x*; comparison of the Seebeck coefficient of pristine $CuFeS_2$ with that of the literature; lattice parameters and room-temperature Hall measurement data of $Cu_{1-x}Sn_xFeS_2$ ($0.0 \leq x \leq 0.1$); Pisarenko plots of Sn substituted $Cu_{1-x}Sn_xFeS_2$ ($0.0 \leq x \leq 0.04$) samples (present work) and that of other substituted $CuFeS_2$ phases in the literature; XPS binding energies and corresponding oxidation states of individual elements in pristine $CuFeS_2$ and Sn-substituted $Cu_{0.96}Sn_{0.04}FeS_2$; SEM images of $Cu_{1-x}Sn_xFeS_2$ ($0.0 \leq x \leq 0.1$) samples showing the various secondary phases; EDS compositions of the main phase in all the samples; EBSD results for $Cu_{0.96}Sn_{0.04}FeS_2$; calculation details of the Lorenz number, mean and average sound velocities, shear and Young's moduli, and Debye temperature (PDF)

■ AUTHOR INFORMATION

Corresponding Author

Anthony V. Powell − *Department of Chemistry, University of Reading, Whiteknights, Reading RG6 6DX, United Kingdom;* ◉ orcid.org/0000-0002-9650-1568; Email: a.v.powell@reading.ac.uk

Authors

Sahil Tippireddy − *Department of Chemistry, University of Reading, Whiteknights, Reading RG6 6DX, United Kingdom*

Feridoon Azough − *Department of Materials, University of Manchester, Manchester M13 9PL, United Kingdom*

Vikram − *Department of Chemistry, University of Reading, Whiteknights, Reading RG6 6DX, United Kingdom;* ◉ orcid.org/0000-0002-5734-6905

Frances Towers Tompkins − *Department of Chemistry, University of Reading, Whiteknights, Reading RG6 6DX, United Kingdom*

Animesh Bhui − *New Chemistry Unit, Jawaharlal Nehru Centre for Advanced Scientific Research, Jakkur, Bangalore 560064, India*

Robert Freer − *Department of Materials, University of Manchester, Manchester M13 9PL, United Kingdom;* ◉ orcid.org/0000-0003-1100-8975

Ricardo Grau-Crespo − *Department of Chemistry, University of Reading, Whiteknights, Reading RG6 6DX, United Kingdom;* ◉ orcid.org/0000-0001-8845-1719

Kanishka Biswas − *New Chemistry Unit, Jawaharlal Nehru Centre for Advanced Scientific Research, Jakkur, Bangalore 560064, India;* ● orcid.org/0000-0001-9119-2455

Paz Vaqueiro − *Department of Chemistry, University of Reading, Whiteknights, Reading RG6 6DX, United Kingdom;* ● orcid.org/0000-0001-7545-6262

Complete contact information is available at:
https://pubs.acs.org/10.1021/acs.chemmater.2c00637

Notes
The authors declare no competing financial interest.

◼ REFERENCES

(1) Freer, R.; Powell, A. V. Realising the Potential of Thermoelectric Technology: A Roadmap. *J. Mater. Chem. C* **2020**, *8*, 441−463.

(2) He, J.; Tritt, T. M. Advances in Thermoelectric Materials Research: Looking Back and Moving Forward. *Science* **2017**, *357*, 1369.

(3) Wei, J.; Yang, L.; Ma, Z.; Song, P.; Zhang, M.; Ma, J.; Yang, F.; Wang, X. Review of Current High-ZT Thermoelectric Materials. *J. Mater. Sci.* **2020**, *55*, 12642−12704.

(4) Zhao, L. D.; Wu, H. J.; Hao, S. Q.; Wu, C. I.; Zhou, X. Y.; Biswas, K.; He, J. Q.; Hogan, T. P.; Uher, C.; Wolverton, C.; Dravid, V. P.; Kanatzidis, M. G. All-Scale Hierarchical Thermoelectrics: MgTe in PbTe Facilitates Valence Band Convergence and Suppresses Bipolar Thermal Transport for High Performance. *Energy Environ. Sci.* **2013**, *6*, 3346−3355.

(5) Wu, Y.; Chen, Z.; Nan, P.; Xiong, F.; Lin, S.; Zhang, X.; Chen, Y.; Chen, L.; Ge, B.; Pei, Y. Lattice Strain Advances Thermoelectrics. *Joule* **2019**, *3*, 1276−1288.

(6) Chang, C.; Wu, M.; He, D.; Pei, Y.; Wu, C. F.; Wu, X.; Yu, H.; Zhu, F.; Wang, K.; Chen, Y.; Huang, L.; Li, J. F.; He, J.; Zhao, L. D. 3D Charge and 2D Phonon Transports Leading to High Out-of-Plane ZT in n-Type SnSe Crystals. *Science* **2018**, *360*, 778−783.

(7) Qin, B.; Wang, D.; He, W.; Zhang, Y.; Wu, H.; Pennycook, S. J.; Zhao, L. D. Realizing High Thermoelectric Performance in p-Type SnSe through Crystal Structure Modification. *J. Am. Chem. Soc.* **2019**, *141*, 1141−1149.

(8) Zhang, C.; de la Mata, M.; Li, Z.; Belarre, F. J.; Arbiol, J.; Khor, K. A.; Poletti, D.; Zhu, B.; Yan, Q.; Xiong, Q. Enhanced Thermoelectric Performance of Solution-Derived Bismuth Telluride Based Nanocomposites via Liquid-Phase Sintering. *Nano Energy* **2016**, *30*, 630−638.

(9) Shin, W. H.; Roh, J. W.; Ryu, B.; Chang, H. J.; Kim, H. S.; Lee, S.; Seo, W. S.; Ahn, K. Enhancing Thermoelectric Performances of Bismuth Antimony Telluride via Synergistic Combination of Multi-

scale Structuring and Band Alignment by FeTe$_2$ Incorporation. *ACS Appl. Mater. Interfaces* **2018**, *10*, 3689−3698.

(10) Powell, A. V. Recent Developments in Earth-Abundant Copper-Sulfide Thermoelectric Materials. *J. Appl. Phys.* **2019**, *126*, 100901.

(11) Xie, H.; Su, X.; Zheng, G.; Zhu, T.; Yin, K.; Yan, Y.; Uher, C.; Kanatzidis, M. G.; Tang, X. The Role of Zn in Chalcopyrite CuFeS$_2$: Enhanced Thermoelectric Properties of Cu$_{1-x}$Zn$_x$FeS$_2$ with In Situ Nanoprecipitates. *Adv. Energy Mater.* **2017**, *7*, 1601299.

(12) Ge, B.; Hu, J.; Shi, Z.; Wang, H.; Xia, H.; Qiao, G. Integration of Multi-Scale Defects for Optimizing Thermoelectric Properties of n-Type Cu$_{1-x}$Cd$_x$FeS$_2$ (x=0-01). *Nanoscale* **2019**, *11*, 17340−17349.

(13) Long, S. O. J.; Powell, A. V.; Vaqueiro, P.; Hull, S. High Thermoelectric Performance of Bornite through Control of the Cu(II) Content and Vacancy Concentration. *Chem. Mater.* **2018**, *30*, 456−464.

(14) Chen, K.; Di Paola, C.; Du, B.; Zhang, R.; Laricchia, S.; Bonini, N.; Weber, C.; Abrahams, I.; Yan, H.; Reece, M. Enhanced Thermoelectric Performance of Sn-Doped Cu$_3$SbS$_4$. *J. Mater. Chem. C* **2018**, *6*, 8546−8552.

(15) Du, B.; Zhang, R.; Chen, K.; Mahajan, A.; Reece, M. J. The Impact of Lone-Pair Electrons on the Lattice Thermal Conductivity of the Thermoelectric Compound CuSbS$_2$. *J. Mater. Chem. A* **2017**, *5*, 3249−3259.

(16) Lu, X.; Morelli, D. T.; Xia, Y.; Ozolins, V. Increasing the Thermoelectric Figure of Merit of Tetrahedrites by Co-Doping with Nickel and Zinc. *Chem. Mater.* **2015**, *27*, 408−413.

(17) Tippireddy, S.; Chetty, R.; Naik, M. H.; Jain, M.; Chattopadhyay, K.; Mallik, R. C. Electronic and Thermoelectric Properties of Transition Metal Substituted Tetrahedrites. *J. Phys. Chem. C* **2018**, *122*, 8735−8749.

(18) He, S.; Luo, Y.; Xu, L.; Wang, Y.; Han, Z.; Li, X.; Cui, J. Remarkable Improvement of Thermoelectric Performance in Ga and Te Cointroduced Cu$_3$SnS$_4$. *Inorg. Chem.* **2021**, *60*, 11120−11128.

(19) Bourgès, C.; Lemoine, P.; Lebedev, O. I.; Daou, R.; Hardy, V.; Malaman, B.; Guilmeau, E. Low Thermal Conductivity in Ternary Cu$_4$Sn$_7$S$_{16}$ Compound. *Acta Mater.* **2015**, *97*, 180−190.

(20) Paradis-Fortin, L.; Guélou, G.; Pavan Kumar, V.; Lemoine, P.; Prestipino, C.; Merdrignac-Conanec, O.; Durand, G. R.; Cordier, S.; Lebedev, O. I.; Guilmeau, E. Structure, Microstructure and Thermoelectric Properties of Germanite-Type Cu$_{22}$Fe$_8$Ge$_4$S$_{32}$ Compounds. *J. Alloys Compd.* **2020**, *831*, 154767.

(21) Suekuni, K.; Kim, F. S.; Nishiate, H.; Ohta, M.; Tanaka, H. I.; Takabatake, T. High-Performance Thermoelectric Minerals: Colusites Cu$_{26}$V$_2$M$_6$S$_{32}$ (M = Ge, Sn). *Appl. Phys. Lett.* **2014**, *105*, 132107.

(22) Candolfi, C.; Guélou, G.; Bourgès, C.; Supka, A. R.; Orabi, R. A. R. A.; Fornari, M.; Malaman, B.; Le Caër, G.; Lemoine, P.; Hardy, V.; Zanotti, J.-M.; Chetty, R.; Ohta, M.; Suekuni, K.; Guilmeau, E. Disorder-Driven Glasslike Thermal Conductivity in Colusite Cu$_{26}$V$_2$M$_6$S$_{32}$ (M = Ge, Sn) Investigated by Mössbauer Spectroscopy and Inelastic Neutron Scattering. *Phys. Rev. Mater.* **2020**, *4*, 025404.

(23) Bouyrie, Y.; Ohta, M.; Suekuni, K.; Kikuchi, Y.; Jood, P.; Yamamoto, A.; Takabatake, T. Enhancement in the Thermoelectric Performance of Colusites Cu$_{26}$A$_2$E$_6$S$_{32}$ (A = Nb, Ta; E = Sn, Ge) Using E-Site Non-Stoichiometry. *J. Mater. Chem. C* **2017**, *5*, 4174−4184.

(24) Freer, R.; Ekren, D.; Ghosh, T.; Biswas, K.; Qiu, P.; Wan, S.; Chen, L. D.; Han, S.; Fu, C.; Zhu, T.-J.; Shawon, A. K. M. A.; Zevalkink, A.; Imasato, K.; Snyder, G. J.; Ozen, M.; Saglik, K.; Aydemir, U.; Cardoso-Gil, R.; Svanidze, E.; Funahashi, R.; Powell, A. V.; Mukherjee, S.; Tippireddy, S.; Vaqueiro, P.; Gascoin, F.; Kyratsi, T.; Philipp, S.; Mori, T. Key Properties of Inorganic Thermoelectric Materials − Tables (Version 1). *J. Phys. Energy* **2022**, *4*, 022002.

(25) Hall, S. R.; Stewart, J. M. The Crystal Structure Refinement of Chalcopyrite, CuFeS$_2$. *Acta Crystallogr., Sect. B: Struct. Crystallogr. Cryst. Chem.* **1973**, *29*, 579−585.

(26) Woolley, J. C.; Lamarche, A.-M.; Lamarche, G.; del Re, R. B.; Quintero, M.; Gonzalez-Jimenez, F.; Swainson, I. P.; Holden, T. M.

Low Temperature Magnetic Behaviour of CuFeSe$_2$ from Neutron Diffraction Data. *J. Magn. Magn. Mater.* **1996**, *164*, 154−162.

(27) Engin, T. E.; Powell, A. V.; Hull, S. A High Temperature Diffraction-Resistance Study of Chalcopyrite, CuFeS$_2$. *J. Solid State Chem.* **2011**, *184*, 2272−2277.

(28) Carr, W. D.; Morelli, D. T. The Thermoelectric Properties and Solubility Limit of CuFeS$_{2(1-x)}$Se$_{2x}$. *J. Electron. Mater.* **2016**, *45*, 1346−1350.

(29) Tsujii, N.; Mori, T. High Thermoelectric Power Factor in a Carrier-Doped Magnetic Semiconductor CuFeS$_2$. *Appl. Phys. Express* **2013**, *6*, No. 043001.

(30) Navratil, J.; Kašparová, J.; Plecháček, T.; Beneš, L.; Olmrová-Zmrhalová, Z.; Kucek, V.; Drašar, Č. Thermoelectric and Transport Properties of n-Type Palladium-Doped Chalcopyrite Cu$_{1-x}$Pd$_x$FeS$_2$ Compounds. *J. Electron. Mater.* **2019**, *48*, 1795−1804.

(31) Xie, H.; Su, X.; Hao, S.; Zhang, C.; Zhang, Z.; Liu, W.; Yan, Y.; Wolverton, C.; Tang, X.; Kanatzidis, M. G. Large Thermal Conductivity Drops in the Diamondoid Lattice of CuFeS$_2$ by Discordant Atom Doping. *J. Am. Chem. Soc.* **2019**, *141*, 18900−18909.

(32) Lefèvre, R.; Berthebaud, D.; Mychinko, M. Y.; Lebedev, O. I.; Mori, T.; Gascoin, F.; Maignan, A. Thermoelectric Properties of the Chalcopyrite Cu$_{1-x}$M$_x$FeS$_{2-y}$ Series (M = Mn, Co, Ni). *RSC Adv.* **2016**, *6*, 55117−55124.

(33) Ge, B.; Shi, Z.; Zhou, C.; Hu, J.; Liu, G.; Xia, H.; Xu, J.; Qiao, G. Enhanced Thermoelectric Performance of n-Type Eco-Friendly Material Cu$_{1-x}$Ag$_x$FeS$_2$ (x=0−0.14) via Bandgap Tuning. *J. Alloys Compd.* **2019**, *809*, 151717.

(34) Park, J.; Xia, Y.; Ozoliņš, V. First-Principles Assessment of Thermoelectric Properties of CuFeS$_2$. *J. Appl. Phys.* **2019**, *125*, 125102.

(35) Tiwari, D.; Chaudhuri, T. K.; Shripathi, T.; Deshpande, U. Synthesis of Earth-Abundant Cu$_2$SnS$_3$ Powder Using Solid State Reaction. *J. Phys. Chem. Solids* **2014**, *75*, 410−415.

(36) Deng, T.; Wei, T. R.; Song, Q.; Xu, Q.; Ren, D.; Qiu, P.; Shi, X.; Chen, L. Thermoelectric Properties of n-Type Cu$_4$Sn$_7$S$_{16}$-Based Compounds. *RSC Adv.* **2019**, *9*, 7826−7832.

(37) Sharma, S. D.; Khasimsaheb, B.; Chen, Y. Y.; Neeleshwar, S. Enhanced Thermoelectric Performance of Cu$_2$ZnSnS$_4$ (CZTS) by Incorporating Ag Nanoparticles. *Ceram. Int.* **2019**, *45*, 2060−2068.

(38) Liang, X.; Wei, X.; Pan, D. Dilute Magnetic Semiconductor Cu$_2$FeSnS$_4$ Nanocrystals with a Novel Zincblende Structure. *J. Nanomater.* **2012**, *2012*, 708648.

(39) Rodríguez-Carvajal, J. FULLPROF: A Program for Rietveld Refinement and Pattern Matching Analysis. In *Abstracts of the Satellite Meeting on Powder Diffraction of the XV Congress of the IUCr*; Toulouse, France, 1990; p 127.

(40) Kresse, G.; Furthmüller, J. Efficiency of Ab-Initio Total Energy Calculations for Metals and Semiconductors Using a Plane-Wave Basis Set. *Comput. Mater. Sci.* **1996**, *6*, 15−50.

(41) Kresse, G.; Furthmüller, J. Efficient Iterative Schemes for Ab Initio Total-Energy Calculations Using a Plane-Wave Basis Set. *Phys. Rev. B* **1996**, *54*, 11169−11186.

(42) Kresse, G.; Hafner, J. Ab Initio Molecular Dynamics for Liquid Metals. *Phys. Rev. B* **1993**, *47*, 558.

(43) Blöchl, P. E. Projector Augmented-Wave Method. *Phys. Rev. B* **1994**, *50*, 17953.

(44) Perdew, J. P.; Burke, K.; Ernzerhof, M. Generalized Gradient Approximation Made Simple. *Phys. Rev. Lett.* **1996**, *77*, 3865−3868.

(45) Dudarev, S. L.; Botton, G. A.; Savrasov, S. Y.; Humphreys, C. J.; Sutton, A. P. Electron-Energy-Loss Spectra and the Structural Stability of Nickel Oxide: An LSDA+ U Study. *Phys. Rev. B* **1998**, *57*, 1505.

(46) Grimme, S.; Antony, J.; Ehrlich, S.; Krieg, H. A Consistent and Accurate Ab Initio Parametrization of Density Functional Dispersion Correction (DFT-D) for the 94 Elements H-Pu. *J. Chem. Phys.* **2010**, *132*, 154104.

(47) Blöchl, P. E.; Jepsen, O.; Andersen, O. K. Improved Tetrahedron Method for Brillouin-Zone Integrations. *Phys. Rev. B* **1994**, *49*, 16223.

(48) Conejeros, S.; Alemany, P.; Llunell, M.; Moreira, I. D. P. R.; Sánchez, V.; Llanos, J. Electronic Structure and Magnetic Properties of CuFeS$_2$. *Inorg. Chem.* **2015**, *54*, 4840−4849.

(49) Martínez-Casado, R.; Chen, V. H. Y.; Mallia, G.; Harrison, N. M. A Hybrid-Exchange Density Functional Study of the Bonding and Electronic Structure in Bulk CuFeS$_2$. *J. Chem. Phys.* **2016**, *144*, 184702.

(50) Eriksson, F.; Fransson, E.; Erhart, P. The Hiphive Package for the Extraction of High-Order Force Constants by Machine Learning. *Adv. Theory Simulations* **2019**, *2*, 1800184.

(51) Plata, J. J.; Posligua, V.; Márquez, A. M.; Sanz, J. F.; Grau-Crespo, R. Fast , Accurate and Non-Empirical Determination of the Lattice Thermal Conductivities of I-III-VI$_2$ Chalcopyrite Semiconductors. *Chem. Mater.* **2022**, *34*, 2833−2841.

(52) Li, W.; Carrete, J.; Katcho, N. A.; Mingo, N. ShengBTE: A Solver of the Boltzmann Transport Equation for Phonons. *Comput. Phys. Commun.* **2014**, *185*, 1747−1758.

(53) Pham, T. D.; Deskins, N. A. Efficient Method for Modeling Polarons Using Electronic Structure Methods. *J. Chem. Theory Comput.* **2020**, *16*, 5264−5278.

(54) Bader, R. F. W. Atoms in Molecules. *Acc. Chem. Res.* **1985**, *18*, 9−15.

(55) Tang, W.; Sanville, E.; Henkelman, G. A Grid-Based Bader Analysis Algorithm without Lattice Bias. *J. Phys. Condens. Matter* **2009**, *21*, No. 084204.

(56) Xie, H.; Su, X.; Zheng, G.; Yan, Y.; Liu, W.; Tang, H.; Kanatzidis, M. G.; Uher, C.; Tang, X. Nonmagnetic in Substituted CuFe$_{1-x}$In$_x$S$_2$ Solid Solution Thermoelectric. *J. Phys. Chem. C* **2016**, *120*, 27895−27902.

(57) Barbier, T.; Berthebaud, D.; Frésard, R.; Lebedev, O. I.; Guilmeau, E.; Eyert, V.; Maignan, A. Structural and Thermoelectric Properties of n-Type Isocubanite CuFe$_2$S$_3$. *Inorg. Chem. Front.* **2017**, *4*, 424−432.

(58) Barbier, T.; Srinivasan, B.; Berthebaud, D.; Eyert, V.; Frésard, R.; Macaigne, R.; Marinel, S.; Lebedev, O. I.; Guilmeau, E.; Maignan, A. Structural Study and Evaluation of Thermoelectric Properties of Single-Phase Isocubanite (CuFe$_2$S$_3$) Synthesized via an Ultra-Fast Efficient Microwave Radiation Technique. *Sustain. Energy Fuels* **2021**, *5*, 5804−5813.

(59) Peng, J.; Fu, L.; Liu, Q.; Liu, M.; Yang, J.; Hitchcock, D.; Zhou, M.; He, J. A Study of Yb$_{0.2}$Co$_4$Sb$_{12}$-AgSbTe$_2$ Nanocomposites: Simultaneous Enhancement of All Three Thermoelectric Properties. *J. Mater. Chem. A* **2014**, *2*, 73−79.

(60) Li, W.; Wang, J.; Poudel, B.; Kang, H. B.; Huxtable, S.; Nozariasbmarz, A.; Saparamadu, U.; Priya, S. Filiform Metal Silver Nanoinclusions to Enhance Thermoelectric Performance of p-Type Ca$_3$Co$_4$O$_{9+\delta}$ Oxide. *ACS Appl. Mater. Interfaces* **2019**, *11*, 42131−42138.

(61) Kumar, A.; Bano, S.; Govind, B.; Bhardwaj, A.; Singh, V. N. Enhanced Thermoelectric Performance of n-Type Zr$_{0.66}$Hf$_{0.34}$Ni$_{1+x}$Sn Heusler Nanocomposites. *J. Alloys Compd.* **2022**, *900*, 163454.

(62) Liu, W.; Tan, X.; Yin, K.; Liu, H.; Tang, X.; Shi, J.; Zhang, Q.; Uher, C. Convergence of Conduction Bands as a Means of Enhancing Thermoelectric Performance of n-Type Mg$_2$Si$_{1-x}$Sn$_x$ Solid Solutions. *Phys. Rev. Lett.* **2012**, *108*, 1−5.

(63) Tang, Y.; Gibbs, Z. M.; Agapito, L. A.; Li, G.; Kim, H. S.; Nardelli, M. B.; Curtarolo, S.; Snyder, G. J. Convergence of Multi-Valley Bands as the Electronic Origin of High Thermoelectric Performance in CoSb$_3$ Skutterudites. *Nat. Mater.* **2015**, *14*, 1223−1228.

(64) Feng, Y.; Li, J.; Li, Y.; Ding, T.; Zhang, C.; Hu, L.; Liu, F.; Ao, W.; Zhang, C. Band Convergence and Carrier-Density Fine-Tuning as the Electronic Origin of High-Average Thermoelectric Performance in Pb-Doped GeTe-Based Alloys. *J. Mater. Chem. A* **2020**, *8*, 11370−11380.

(65) Nakai, I.; Sugitani, Y.; Nagashima, K.; Niwa, Y. X-Ray Photoelectron Spectroscopic Study of Copper Minerals. *J. Inorg. Nucl. Chem.* **1978**, *40*, 789−791.

(66) Ghahremaninezhad, A.; Dixon, D. G.; Asselin, E. Electrochemical and XPS Analysis of Chalcopyrite ($CuFeS_2$) Dissolution in Sulfuric Acid Solution. *Electrochim. Acta* **2013**, *87*, 97−112.

(67) Li, Y.; Zhang, T.; Qin, Y.; Day, T.; Jeffrey Snyder, G.; Shi, X.; Chen, L. Thermoelectric Transport Properties of Diamond-like $Cu_{1-x}Fe_{1+x}S_2$ Tetrahedral Compounds. *J. Appl. Phys.* **2014**, *116*, 203705.

(68) Murr, L. E.; Lerner, S. L. Transmission Electron Microscopic Study of Defect Structure in Natural Chalcopyrite ($CuFeS_2$). *J. Mater. Sci.* **1977**, *12*, 1349−1354.

(69) Callaway, J. Model for Lattice Thermal Conductivity at Low Temperatures. *Phys. Rev.* **1959**, *113*, 1046−1051.

(70) Callaway, J.; von Bayer, H. C. Effect of Point Imperfections on Lattice Thermal Conductivity. *Phys. Rev.* **1960**, *120*, 1149−1154.

(71) Slack, G. A. Effect of Isotopes on Low-Temperature Thermal Conductivity. *Phys. Rev.* **1957**, *105*, 829.

(72) Abeles, B. Lattice Thermal Conductivity of Disordered Semiconductor Alloys at High Temperatures. *Phys. Rev.* **1963**, *131*, 1906−1911.

(73) Hashikuni, K.; Suekuni, K.; Watanabe, K.; Bouyrie, Y.; Ohta, M.; Ohtaki, M.; Takabatake, T. Carrier Concentration Tuning in Thermoelectric Thiospinel $Cu_2CoTi_3S_8$ by Oxidative Extraction of Copper. *J. Solid State Chem.* **2018**, *259*, 5−10.

(74) Zhang, D.; Zhang, B.; Zhou, Z.; Peng, K.; Wu, H.; Wang, H.; Wang, G.; Han, G.; Wang, G.; Zhou, X.; Lu, X. Ultralow Lattice Thermal Conductivity of Cubic $CuFeS_2$ Induced by Atomic Disorder. *Chem. Mater.* **2021**, *33*, 9795−9802.

(75) Ge, B.; Lee, H.; Zhou, C.; Lu, W.; Hu, J.; Yang, J.; Cho, S.-P.; Qiao, G.; Shi, Z.; Chung, I. Exceptionally Low Thermal Conductivity Realized in the Chalcopyrite $CuFeS_2$ via Atomic-Level Lattice Engineering. *Nano Energy* **2022**, *94*, 106941.

(76) Guilmeau, E.; Barbier, T.; Maignan, A.; Chateigner, D. Thermoelectric Anisotropy and Texture of Intercalated TiS_2. *Appl. Phys. Lett.* **2017**, *111*, 133903.

(77) Rathore, E.; Juneja, R.; Culver, S. P.; Minafra, N.; Singh, A. K.; Zeier, W. G.; Biswas, K. Origin of Ultralow Thermal Conductivity in n-Type Cubic Bulk $AgBiS_2$: Soft Ag Vibrations and Local Structural Distortion Induced by the Bi $6s^2$ Lone Pair. *Chem. Mater.* **2019**, *31*, 2106−2113.

(78) Chmielowski, R.; Péré, D.; Bera, C.; Opahle, I.; Xie, W.; Jacob, S.; Capet, F.; Roussel, P.; Weidenkaff, A.; Madsen, G. K. H.; Dennler, G. Theoretical and Experimental Investigations of the Thermoelectric Properties of Bi_2S_3. *J. Appl. Phys.* **2015**, *117*, 125103.

(79) Wang, L.; Ying, P.; Deng, Y.; Zhou, H.; Du, Z.; Cui, J. Site Occupations of Zn in $AgInSe_2$-Based Chalcopyrites Responsible for Modified Structures and Significantly Improved Thermoelectric Performance. *RSC Adv.* **2014**, *4*, 33897−33904.

(80) Ohta, M.; Chung, D. Y.; Kunii, M.; Kanatzidis, M. G. Low Lattice Thermal Conductivity in $Pb_5Bi_6Se_{14}$, $Pb_3Bi_2S_6$, and $PbBi_2S_4$: Promising Thermoelectric Materials in the Cannizzarite, Lillianite, and Galenobismuthite Homologous Series. *J. Mater. Chem. A* **2014**, *2*, 20048−20058.

(81) Song, Q.; Qiu, P.; Zhao, K.; Deng, T.; Shi, X.; Chen, L. Crystal Structure and Thermoelectric Properties of $Cu_2Fe_{1-x}Mn_xSnSe_4$ Diamond-like Chalcogenides. *ACS Appl. Energy Mater.* **2020**, *3*, 2137−2146.